DOI: 10.13009/EUCASS2019-346



# Development of a functionally graded material for new combustion chambers at ultra-high temperature under oxidising atmosphere

***L. Sévin****[bc], A. Julian-Jankowiak[*], J.-F. Justin[*], L. Vingert[*], P. Bertrand[b], C. Langlade[b], N.Pelletier[d]

[*] ONERA– Université de Paris-Saclay, F-92322 Châtillon, France.
(louise.sevin@onera.fr; aurelie.jankowiak@onera.fr; jean-francois.justin@onera.fr; lucien.vingert@onera.fr)

[b] ICB, Université de Bourgogne, Franche-Comté, Sevenans, 90400, France.
(cecile.langlade@utbm.fr; pierre.bertrand@utbm.fr)

[c] Direction des Systèmes Orbitaux, CNES, Toulouse, 31410, France.

[d] ONERA– Université de Toulouse, F-31055 Toulouse, France
(nicolas.pelletier@onera.fr)

**Abstract**

CNES, ONERA and ICB-PMDM have collaborated to develop a Functionally Graded Material (FGM) with two different materials selected for their refractory properties: a ceramic as environmental and thermal barrier and a metal as structural part. Besides the fact that over the application's temperature range, the thermal expansion is twice higher for the ceramic, there is no delamination in the FGM elaborated by plasma spraying process. This is still the case after thermal cycling under inert atmosphere at 2073 K and after undergoing a parietal heat flow in a burner ring facility (flame up to 2300 K / 10 bar).

DOI: 10.13009/EUCASS2019-346



## 1. Introduction

Anhydrous hydrazine, widely used as monopropellant in spacecraft thrusters, has been declared as suspected toxic, mutagen and carcinogen for humans and could be prohibited by the European Regulations REACh in the 2020s. Thereby, CNES has engaged the development of a new low-toxicity and high performance "green" monopropellant inducing harsh operating conditions. Indeed, the flame temperature will be increased up to 3000 K with oxidising combustion gases. Moreover, to further optimise engine performance, no film cooling will be used. Thus, these two demanding specifications induce the development of new materials.

Most of studies dedicated to the development of material for chemical combustion thrusters were realised in the nineties to replace the silicide coated niobium chamber whose use was limited to 1643K [1]. Studies reported tests with oxidative flame on cooling or non-cooling chamber configurations and pointed out that metallic chambers made of iridium coated rhenium have better performance than ceramic matrix composites such as SiC/SiC (limited to 1973K due to the protective silica film which degrades rapidly) [1]. Also, the addition of a ceramic oxide overlayer on the inner surface of iridium/rhenium chambers has been reported to significantly improve their oxidation resistance [2,3], thereby allowing more oxidising operating conditions, higher temperatures, and enhanced life up to 2473K. However these chambers also had some defects such as rhenium diffusion into iridium layer and spalling of the ceramic coating [4–6] or very limited time and number of cycles before total failure [7]. Besides this, its seem that a thicker ceramic oxide layer (~850µm) would be more impermeable to oxygen, but present more macro-cracking, than a thinner one (~25µm), suiting better for repeated thermal cycling [8].
More recently, an Iridium-Aluminium intermetallic as material for ablation resistance showed very interesting properties [9,10].

CNES, ONERA and ICB-PMDM have been working for several years in close collaboration on the designing of such a tough material. To fulfil functional specifications, the development was oriented on the processing of a Functionally Graded Material (FGM) instead of duplex coating (Figure 1). Two ultra-refractory materials were selected: one is a ceramic oxide which can handle oxidative environments and very high operating temperatures (up to its melting point 3031K) but with relatively poor mechanical properties compared to the second material. Indeed, the structural part is made of a refractory metal with high melting point but low oxidation resistance. It is important to notice that these two complementary materials have a significant difference of their average thermal expansion coefficient over a wide range of temperature (>$5.10^{-6}$ $K^{-1}$ between 293 and 2273K). Even though, the average thermal expansion of the stabilised hafnia [11] is higher than those of the metal, the latter was preferred to a monoclinic hafnia to avoid the cubic to monoclinic transformation leading to a volume expansion about 3% [12]. Thanks to its gradual thermomechanical properties change, the objective of the intermediate layer is to smooth materials properties differences, such as thermal expansion (mismatches generally lead to high levels of thermal stresses). Thus, this solution allows *in fine* to bring down the spalling between layers [13–16].

Among the wide range of techniques used to elaborate FGM [17], the Air Plasma Spraying (APS) process was selected. Widely used to obtain Thermal Barrier Coatings (TBCs) [18,19] and Environmental Barrier Coatings (EBCs)[20], it is also applied to manufacture complex shapes. Thanks to the microstructure brought by this process as porosities and micro cracks, it allows to reduce thermal conductivity and thus, to improve thermal shock and thermal cycling performances [21]. The graded multi-layered materials have been designed and processed in a manner to prevent, for these first tests, delamination during thermal loading in service conditions. In this way, design criteria were based on minimising radial constraints [22–24].

This paper presents the elaboration of several innovative material solutions for combustion chambers and their behaviour under two different thermal cycling tests. One carried out on a $CO_2$ laser facility under vacuum and the other with a burner ring under representative atmosphere and pressure. The effect of several parameters such as ceramic thickness and temperature of thermal treatment on cracks morphology will be discussed.

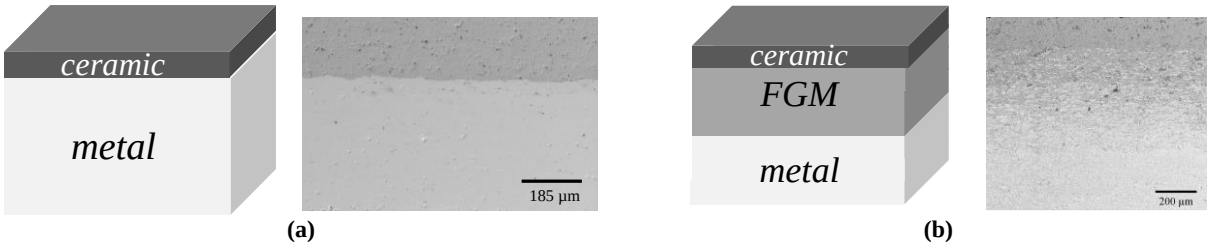


**(a)** **(b)**

**Figure 1 : Schematics and micrographs of an as-sprayed duplex coating (a) and a FGM (b) for combustion chambers**

DOI: 10.13009/EUCASS2019-346

## 2. Experimental procedures

### 2.1. Specimen preparation

Ceramic/metal functionally graded systems were atmospheric plasma sprayed with Yttria Stabilised Hafnia from Marion Technologies (12%mol. $Y_2O_3$ with $D_{50}$=1µm) for EBC/TBC layer and metallic powders for the structural layer. The large density difference of these two compounds leads to unequal penetration trajectories into the plasma plume. Therefore, instead of only controlling the rates of two pure powder feeders [25,26], pre-alloyed composite powders were used to obtain intermediate compositions and a final homogeneous and continuous FGM material with different spraying parameters. Characteristics of samples are summarised in Table 1, showing that several thicknesses of ceramic layer were elaborated to be tested and compared as well as the FGM transition. Systems comprise between 5 and 7 graded layers mostly based on the optimisation design results linked to the different ceramic thicknesses used but also on the process feasibility. In any case, it was enough to obtain a continuous FGM layer in which it was difficult to identify and measure the thickness of each layer.

**Table 1: Graded structures and sizes of coatings after Consolidation Thermal Treatments (CTT)**

| | | Type-A | Type-B | Type-C | Type-D | Type-E | Type-F |
|---|---|---|---|---|---|---|---|
| | Ref. ONERA | PBTT | PCTT | Config.1 | Config.2 | Config.3 | Config.4 |
| Thickness (µm) | YSH | 206 | 379 | 192 | 179 | 159 | 65 |
| | FGM | 448 | 589 | 563 | 534 | 452 | 488 |
| | Metal | 557 | 561 | 1242 | 1223 | 1024 | 980 |
| CTT (K) | | 2273 | 2273 | 2273 | 2273 | 1873 | 2273 |
| FGM transition | | soft | soft | steep | soft | soft | soft |

Materials were sprayed onto different kinds of substrates shown on Figure 2. For $CO_2$ laser tests, molybdenum pieces of 20mm diameter were used because of their dissolution property in cold diluted nitric acid (Figure 2 (a)). For Mascotte tests, specific pieces which can be screwed in the sample holder were made in the same metal than the selected structural layer to have the same thermal properties than the first layer and to avoid delamination during CTT (Figure 2 (b)).
Before deposition, all the substrates were grit-blasted using alumina balls.

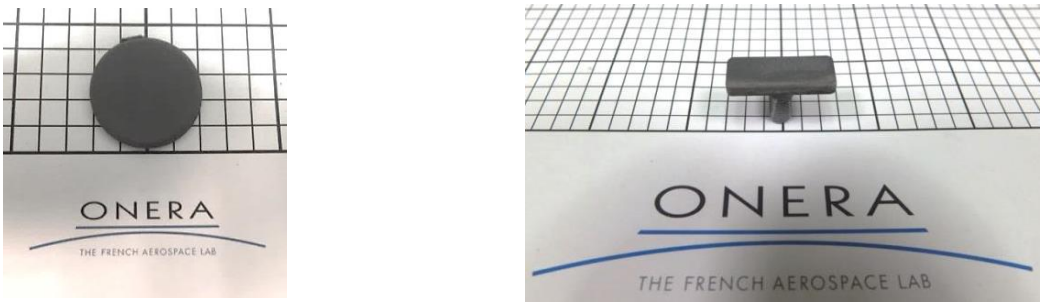


**(a)** **(b)**

**Figure 2 : Macrographs of a $CO_2$ laser test sample (a) and a Mascotte test bench sample (b)**

The use of thermal spray under air (APS) was motivated by its practicality, the good management of substrate temperature and the great coating ceramic quality compared to vacuum one (VPS). However it leads to a partial oxidation of the melted metal powder during the transport from the plasma plume to the substrate bringing to intersplat oxide species and splat decohesion. Thanks to some thermodynamic calculations of oxides stability (HSC Chemistry v8.0), an appropriate thermal treatment was applied to eliminate metal oxides and consolidate the material (Figure 3). Two heat treatment temperatures were investigated to study their influence on the microstructure and on the overall performances under thermal cycling (samples characteristics in Table 1).

Microstructures of both as-processed and thermally treated materials were analysed by Scanning Electron Microscopy on cross-sectioned samples and the Energy Dispersive X-ray analyser was used for X-ray maps.

DOI: 10.13009/EUCASS2019-346



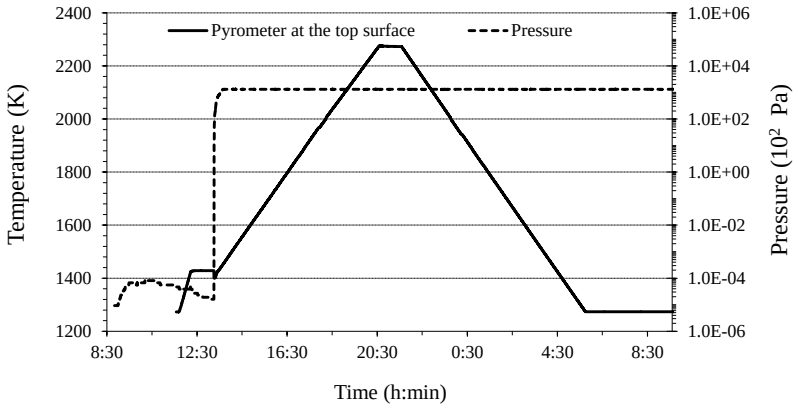


**Figure 3 : Typical consolidation thermal treatment to release metal oxides**

## 2.2. $CO_2$ laser test bench

The heat flow is imposed at the centre of the top surface of a sample by a high power continuous $CO_2$ laser beam (3kW) as represented in Figure 4 (a). The heat flow distribution provided on the specimen surface by the laser was found to be Gaussian shaped. For each sample, a preliminary test was used to optimise the required power to reach the targeted temperature given by a mono (1µm) and a bi-chromatic pyrometer (0.9 and 1 µm). The measured emissivity was closed to the one given by Del Campo *et al.* (ε~0.55 at 2170K), respectively between 0.55 and 0.75 for the tested samples and was highly dependent on their roughness [27]. The thermal cycle controlled by the power allows avoiding power peaks during test on FGM that could happen with a temperature monitored mode when there are surface modifications as spallation or oxidation. This test bench was used to subject samples to thermal cycling and also to evaluate their thermal shock behaviour (in primary vacuum to avoid the oxidation of metal).
For thermal cycling tests, a ramp of 8 W/s and a maximal power of 200 W leading to a maximum temperature of 2093 K and a heat flow of 1.13 MW/m² were reached in 25 s and applied during 100 s. This cycle was repeated three times with a cooling step down to ambient temperature between each cycle as shown in Figure 5 (a).
For the thermal shock tests, a cycle with a maximum temperature of 2300 K corresponding to a maximum laser flux of 2.15 MW/m² was obtained in 33 s and maintained during 100 s (Figure 5 (b)).
For both of these thermal tests, post-test SEM and optical examinations of the cross-section of samples were analysed. Considering such thermal and atmosphere conditions, no continuous analyses were possible.

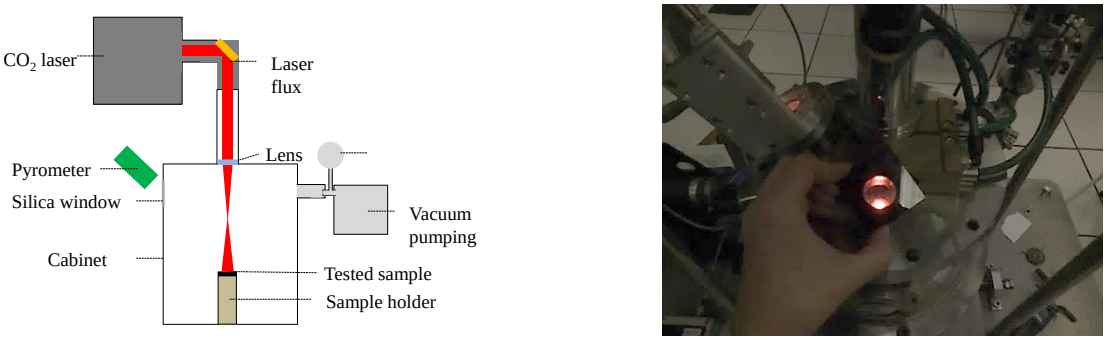


**(a) Schema of the $CO_2$ laser test bench** **(b) View during the heating step of a thermal cycle**

**Figure 4: The $CO_2$ laser test bench : (a) schematic view, (b) observation of the heated sample during a test**

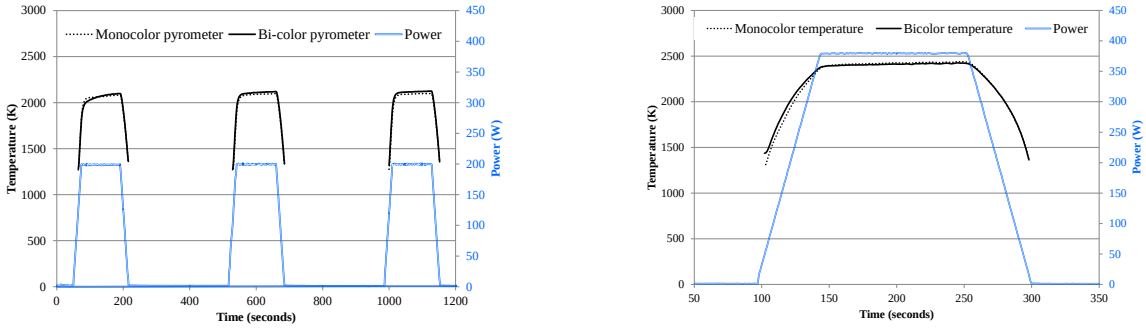


**(a)** **(b)**

**Figure 5: Typical temperatures and power ramps during test (a) thermal cycle, (b) thermal shock**

## 2.3. Mascotte test bench

The Mascotte bench is a large facility. Its biggest part is dedicated to the management of the oxidiser ($O_{2(g)}$ or $O_{2(l)}$), the fuel ($H_{2(g)}$ or $CH_{4(g)}$) and the servitude fluids (He, $N_2$, $LN_2$, $H_2O$). The core of the facility is the "reactor box" of which several versions were developed to answer to specific fields of research (*e.g.* atomisation-combustion, new propellants assessment, over expanded nozzles, ignition, high frequency instabilities, etc.). Indeed, this bench was originally dedicated to combustion studies and for the first time, Mascotte is used to investigate the performances of materials. Thus a significant part of the study was dedicated to the design of a specific samples holder which allows tightness of the chamber enduring 10 bar Figure 6 (a). It also had to be non oxidisable with high calorific capacity and high melting point (copper was selected). In this case, Mascotte uses the high pressure-high mixing ratio box (Bhp-HrM) (Figure 6 (b)). This chamber is made of steel (melting temperature of ~1700K). Several temperatures flames were tested thanks to oxygen and hydrogen flows variations as 1500, 2000 and 2300K. The test bench is modular and for the two firsts operating points, the samples holder was placed close to the injector, just after the flame and thus exposed to combustion products, essentially $H_2O$, $H_2$, OH (Table 2) and some ionic products. For the highest operating point, we have met some facility issues and besides the great behaviour of the FGM samples, the samples holder was moved away from the flame to avoid melting of the chamber.
Instrumentation on this kind of facility is complicated. In this case, samples were weighted and measured before and after each tests, and the surface observed by a binocular. Post-test observations consisted of SEM and optical cross-section observations of samples and the analyses of cracks morphology by an image analysis with Image J on optical micrographs.

Each firing time is constituted of a primary step of ignition during 10 s and a second step of test during 15 s. During the first step, samples are subjected to a high temperature flame and thus, to a severe thermal shock as shown in Figure 8. The effective test period is during the stable step with desired temperature flame and thus previous calculated products species. Throughout the shot, materials endure 25 s of high temperature flame and oxidising products under a pressure of 10 bar. Each sample was exposed to the flow 100 s (cumulated time).

**(a) View of the samples holder (2 samples/ 4 thermal fluxmeters)** **(b) View of the Mascotte test bench**

**Figure 6: Mascotte facility in materials performance test conditions**

DOI: 10.13009/EUCASS2019-346



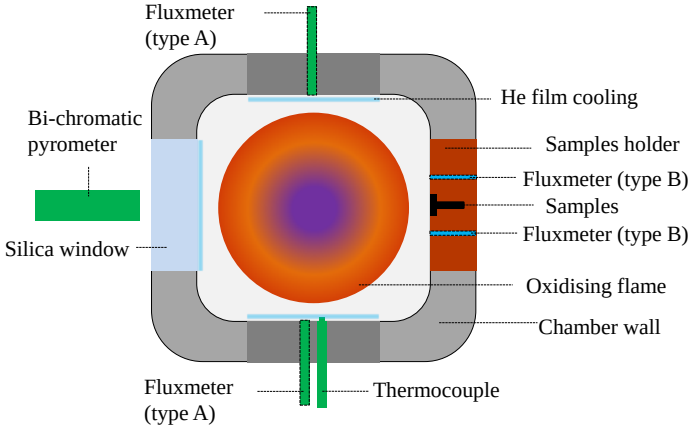


**Figure 7: Schematic cross-section view of the Mascotte facility**

**Table 2: Calculated equilibrium flame temperatures and average quantities of produced species (without He film cooling) bringing by pre-defined reactants proportions**

| | Mass fraction | | | |
|---|---|---|---|---|
| Flame temperature (K) | $H_2O$ | $H_2$ | $OH^-$ | $H^+$ |
| 1500 | 0.64 | 0.36 | - | - |
| 2000 | 0.74 | 0.26 | $3.9.10^{-5}$ | $7.5.10^{-5}$ |
| 3000 | 0.79 | 0.21 | $3.8.10^{-4}$ | $3.5.10^{-4}$ |

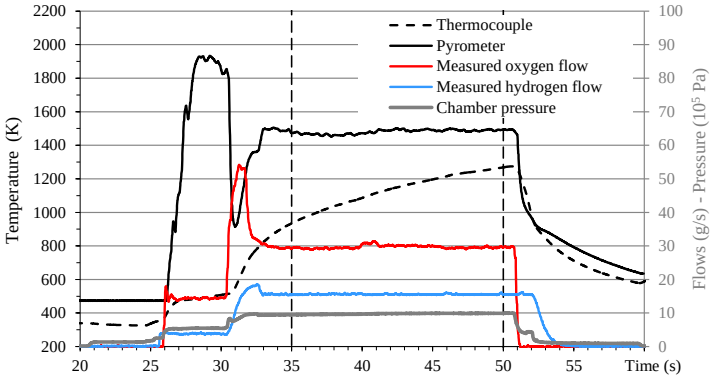


**Figure 8 : Evolution of temperatures, pressure and gas flows during a test with a temperature flame of 2000 K**

## 3. Results

### 3.1. Microstructure of as-processed FGM

As–processed samples with the largest and thinnest ceramic thicknesses respectively Figure 9 (a) and (b) show micro cracks and porosity which are typical microstructures of Air Plasma Sprayed materials [28]. They also contain some unmelted particles related to a non-sufficient calorific plasma plume. Most of the porosity in the specimen type F comes from the pull out of some splats during the polishing step. They both show an homogeneous microstructural transition in the FGM layers where the microstructure is characterised by the gradual change replacement from pure metal at the bottom, then metal matrix to ceramic matrix and then pure ceramic with increase in the fraction of ceramic phase from the bottom to the top surface. This is noticeable by the grey nuances in Figure 9 thanks to the difference of the molar mass of YSH and the metal and in the X quantitative elements maps in Figure 10.

DOI: 10.13009/EUCASS2019-346

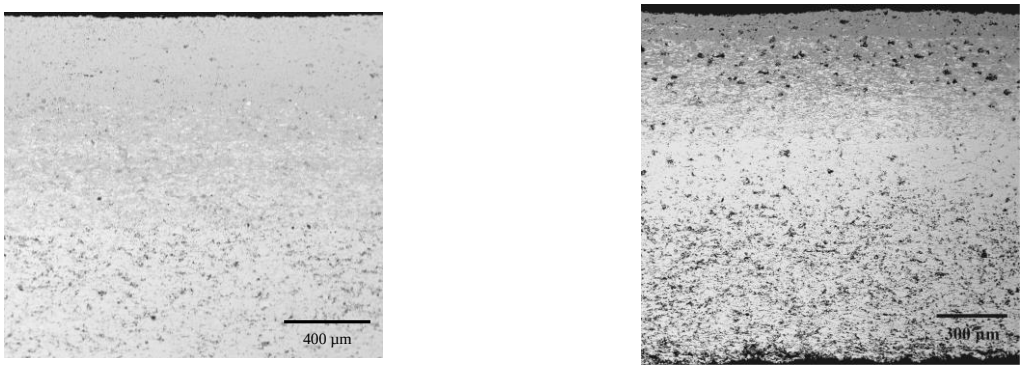


**(a) Type B** **(b) Type F**

**Figure 9: SEM images of cross-sections of as sprayed materials with two different ceramic thicknesses (respectively 379 and 65 µm)**

The Figure 10 allows assessing the homogenous gradient layer. Indeed, it is difficult to distinguish each type of layers. There is a good adhesion providing high quality of deposition and no delamination obsvered between each layer. The analyse of SEM observation and metal and oxygen maps highlighted that sample presents some porosities and that the oxygen is present in the metal layer in two different forms as metal oxides between metal spats, and as a pollution (analysed as $Al_2O_3$ particles from sample holder). Also, the ceramic layer seems to contain different and inhomogeneous amount of yttrium in Yttria Stabilized Hafnia (YSH) particles bringing different thermo-mechanical properties.

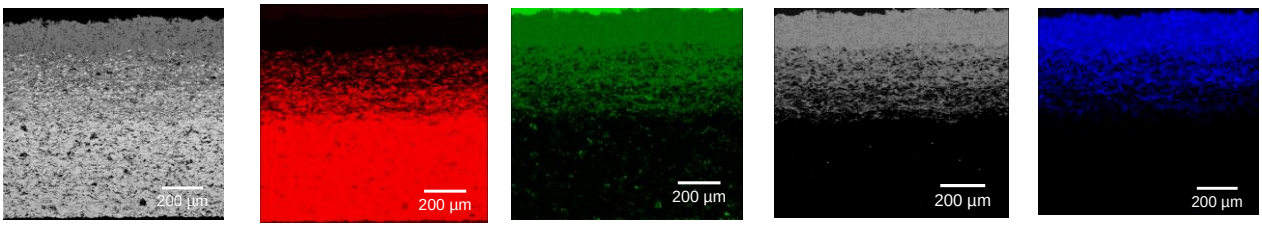


**(a) BSE** **(b) Me** **(c) O** **(d) Hf** **(e) Y**

**Figure 10: SEM observation and X-ray quantitative maps of each elements of the as-processed type A material**

3.2. Materials after thermal consolidation

A specific thermal treatment (Figure 3), which had as first aim to eliminate metal oxides, was applied to the samples. Indeed, Figure 11 (b) indicates clearly the presence of metal oxides at the inter-splat area. After the thermal treatment the oxygen X-ray map does not show any content of oxygen Figure 11 (c).

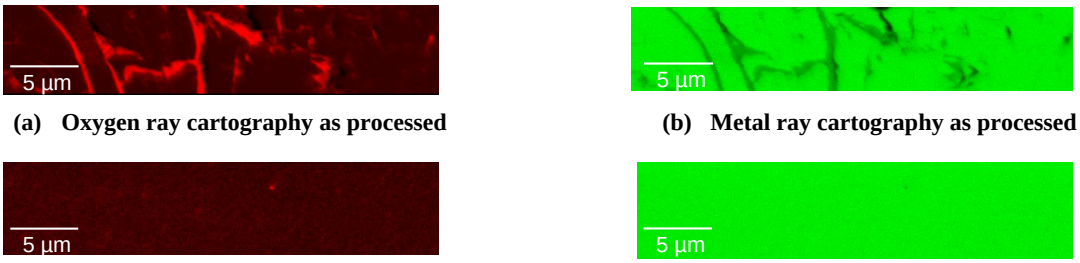


**(a) Oxygen ray cartography as processed** **(b) Metal ray cartography as processed**

**(c) Oxygen ray cartography after thermal treatment** **(d) Metal ray cartography after thermal treatment**

**Figure 11: EDX cartography of metal layer as processed (a) oxygen (b) metal and after thermal treatment (c) oxygen (d) metal.**

Moreover, an analysis concerning the distribution of metal and hafnium still shows a homogeneous gradient without any element diffusion and good adhesion between layers (Figure 12).

DOI: 10.13009/EUCASS2019-346



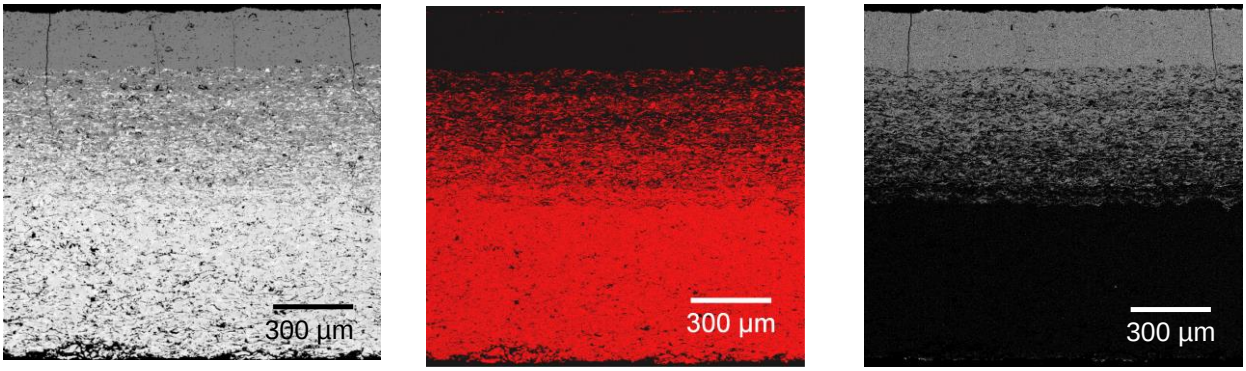


(a) SEM (b) Me (e) Hf

**Figure 12: SEM and EDX cartography of a thermally treated sample (type A)**

This thermal treatment also points out that compared to duplex coatings (Figure 13 (a)), functionally graded samples does not show neither horizontal cracks nor delamination which indicates a potential improvement of life (no spallation behaviour). However, thermally activated time dependent viscoplastic phenomenons, sintering, stress-relaxation and creep lead to tensile loads [29] and causes the initiation and growth of surface cracks also known as vertical cracks Figure 13 (b) and (c).

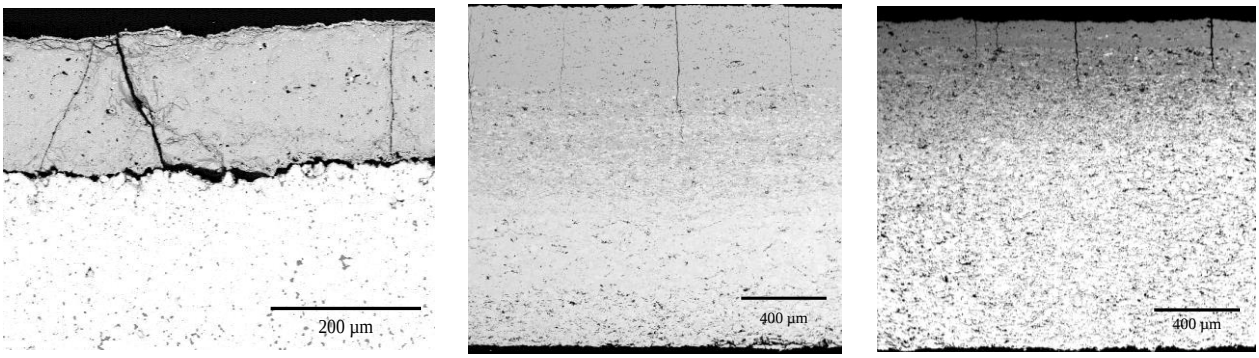


**(a) Duplex coating** **(b) Type B** **(c) Type F**

**Figure 13: Comparison between duplex and FGM samples after TTC**

The effect of ceramic thickness and temperature of the thermal treatment on the normalised crack length (ratio of cracks length to the ceramic thickness) and on the normalised cracks spacing (ratio of cracks spacing to the ceramic thickness) were studied and respectively reported in Figure 14 and Figure 15.

Figure 14 shows that regardless of the ceramic thickness all cracks go through the ceramic layer and reach the FGM layer. However, some linear conclusions can be draw from this study. The smallest the ceramic thickness, the largest the normalised cracks length is. It is also possible to conclude that the smallest the ceramic thickness, the largest the normalised cracks spacing is.

Comparing samples with different temperatures of thermal treatment, a lower temperature seems to lead to a FGM with longer and more distant normalised cracks.

From these analyses it is really difficult to discriminate a design for ceramic thickness or for the temperature of the thermal treatment because of the large error type bars on the results recorded just right after the thermal treatment. It is important to keep in mind that surface crack propagation is induced by sintering, creep and thermal expansion mismatch.

DOI: 10.13009/EUCASS2019-346

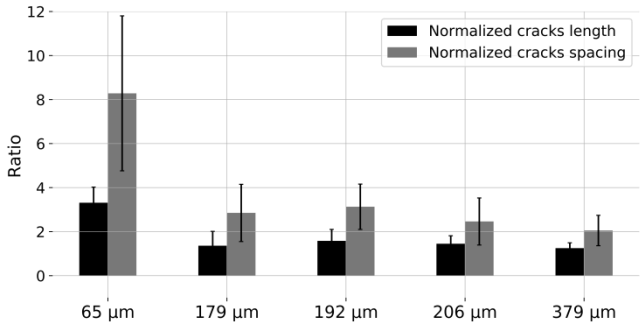


**Figure 14: Normalised cracks length and cracks spacing to ceramic thickness for different ceramic thicknesses (samples after thermal treatment)**

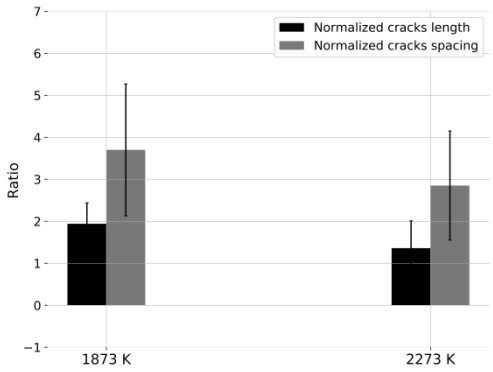


**Figure 15: Normalized cracks length and cracks spacing to ceramic thickness for two different temperatures of the thermal treatment**

### 3.3. Thermal fracture behaviour under inert atmosphere

To study the performance of samples with two different ceramic thicknesses under thermal cycling and thermal shock, a heating flux provided by a $CO_2$ laser was used. Tests were carried out under vacuum to overcome the metal oxidation which would be predominant without a specific sample holder to protect the lateral sides of the cylindrical sample.

**Figure 16** shows typical damages observed in samples type A and type B after thermal treatment, thermal cycling at 2093K and thermal shock at 2300K. The SEM examinations of the cross-sections of samples point out the vacancy of horizontal cracks or delamination after thermal treatment, and thermal cycling. However, after thermal shock at high temperature (2300K), in sample type A, it appears some short deflected cracks in the dense part of the metal layer in the direction parallel to the surface. Both samples have generated vertical cracks propagating through the ceramic thickness which reach the graded layer.

DOI: 10.13009/EUCASS2019-346



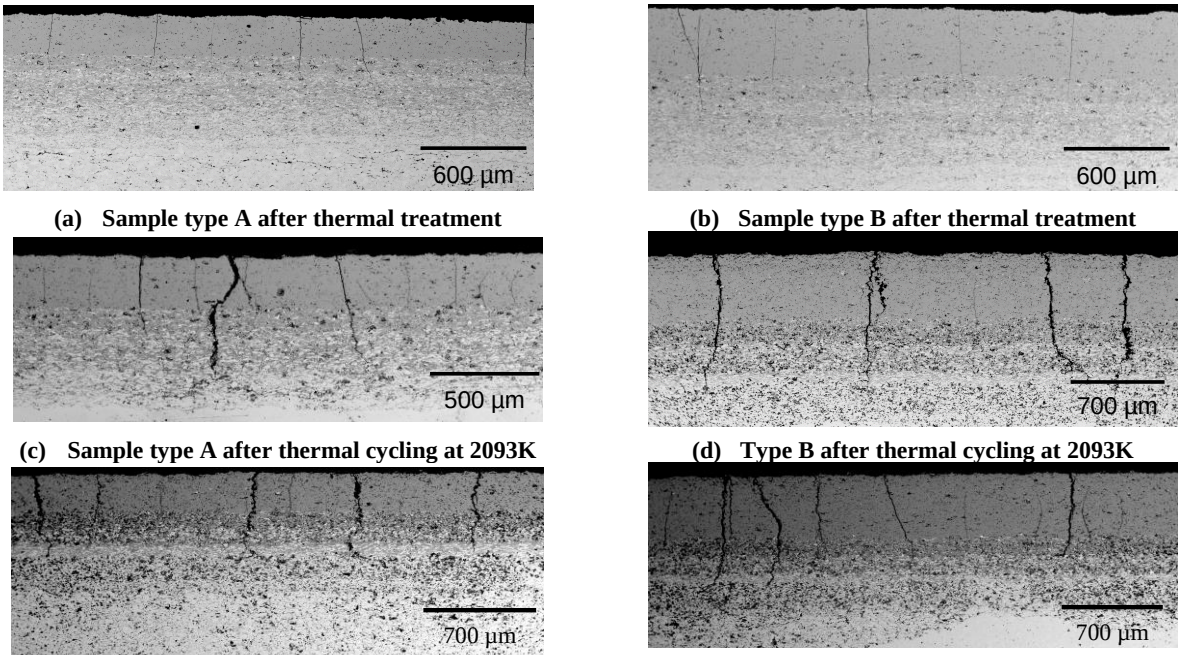


**(a) Sample type A after thermal treatment**

**(b) Sample type B after thermal treatment**

**(c) Sample type A after thermal cycling at 2093K**

**(d) Type B after thermal cycling at 2093K**

**(e) Type A after thermal shock at 2300K**

**(f) Type B after thermal shock at 2300K**

**Figure 16: Microstructure observation by SEM of samples after thermal treatment for type A (a) and type B (b), after thermal cycling at 2093 K for type A (c) and type B (d), and after thermal shock at 2300K type A (e) and type B (f)**

This kind of fracture behaviour has been extensively reported in TBC, EBC and FGM thermal cycling studies [13,29–31] allowing an explanation of the phenomenon. The numerical analysis carried under Comsol Multiphysics ® a cylindrical sample submitted to a heating step from ambient temperature to 2273K and a cooling from 2273K to ambient temperature with 3 different ceramic thicknesses is presented Figure 17. The resultant constraints during heating point out that the top surface of samples is in large compressive stress state. During cooling, the resulting strain becomes tensile. The change from compression to tension seems large enough to overcome the fracture strength of YSH and causes vertical cracks. For larger ceramic thicknesses, it seems that the higher tensile stresses do not occur at the shallow surface contrary to thinner ceramic layers and that their tensile magnitudes are lower.

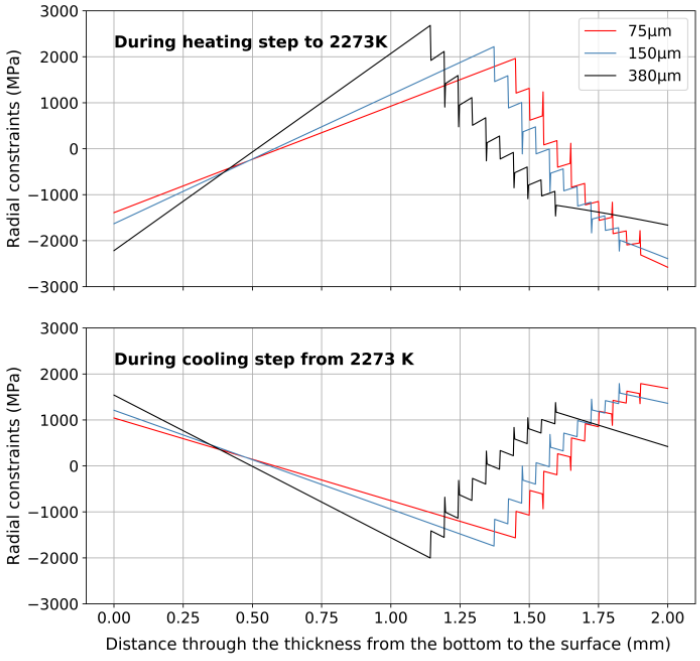


**Figure 17: Visualisation of the compression load during heating process and tension load during cooling process**

DOI: 10.13009/EUCASS2019-346

The vertical cracks correspond to a mode I and the related stress intensity decreases as the crack extends into the material. However cracks which deflect toward the direction parallel to the surface correspond of mode II stress intensity. Thus, it seems possible to control the crack propagation by keeping the stress intensity factors of the mode II equal to zero. That could be possible by designing the optimised layers composition.

### 3.4. Material behaviour under service atmosphere and pressure

The Mascotte facility has been used to show off under representative atmosphere (water vapour) and pressure the design parameters which have an impact on the performance of FGM. Samples type D have been identified as reference samples. All the other samples of this batch have only one difference with these latter. Type C has a FGM with a steep transition compared to type D, while type E has been thermally treated with a different maximum temperature (1873K), and type F with a different ceramic thickness. It was also the opportunity to check the impact of the vertical cracks on the oxidation that it is known to promote spallation [32].
After tests, all the samples show neither size nor mass variation and the top surface of samples studied thanks to a binocular does not show any spallation.
Before the limitation of the facility, the reference samples could be tested at the highest temperature flame allowing the comparison of its microstructure and cracks propagation for all temperature flame.

Thus, as shown in Figure 18, cross-section microstructure observations of samples type D display only vertical cracks. Given that there is no oxidation of the metal part, and no oxide formation during these thermal cycles, besides the presence of verticals cracks through the ceramic layer to the graded layer composed of metal, it can be concluded that for this limited duration of test, they are not detrimental on the lifetime under oxidant atmosphere. Moreover, this kind of vertical cracks is effective in reducing thermal stresses without changing the heat resistance of samples and so the design of functionally graded material must include verticals cracks while controlling their propagation to prevent spallation [33].

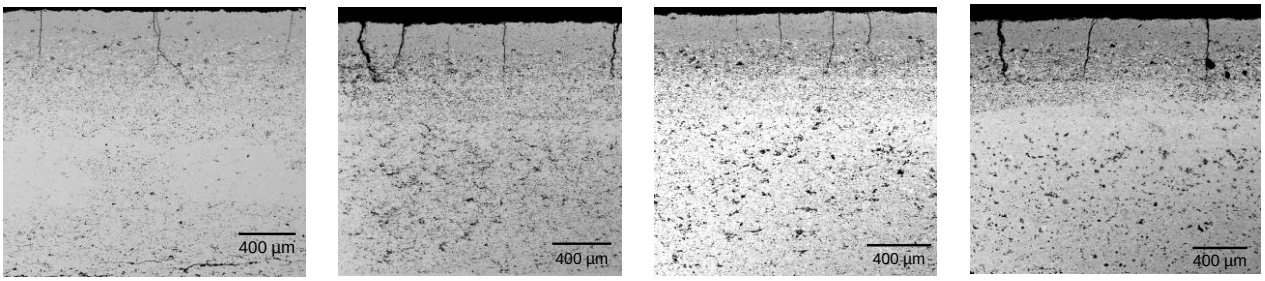


**(a) After TT** **(b) After Mascotte-1500K** **(c) After Mascotte-2000K** **(d) After Mascotte-2300K**

**Figure 18: Microstructure observations by SEM of samples type D after thermal treatment (a), after Mascotte cycling at flame temperature of 1500K (b), after Mascotte cycling at flame temperature of 2000K (c), after Mascotte cycling at flame temperature of 2300K (d)**

For the sake of brevity, the comparison between the reference samples and the other has been carried out for a flame temperature of 2000K.

In comparison to a soft FGM transition, having a steep transition seems to bring larger and more distant normalised cracks than the reference samples as-thermally treated (Figure 19 (a)). After test at the operating atmosphere condition, the type D seems more sensitive and is subjected to more progression of these cracks, longer and closest. It is important to note that after test, cracks have a wide dispersion in terms of length and distance between them.
Then the comparison between samples with different temperatures of thermal treatment (Figure 19 (b)) pointed out that besides a lower thermal treatment temperature, the sample seems to have longer but more distant cracks. The low progression after thermal cycles of normalised cracks for type E could involve a better resistance to thermal cycling than type D. The sample with the thinnest ceramic layer has the longest and distant normalised cracks.

DOI: 10.13009/EUCASS2019-346



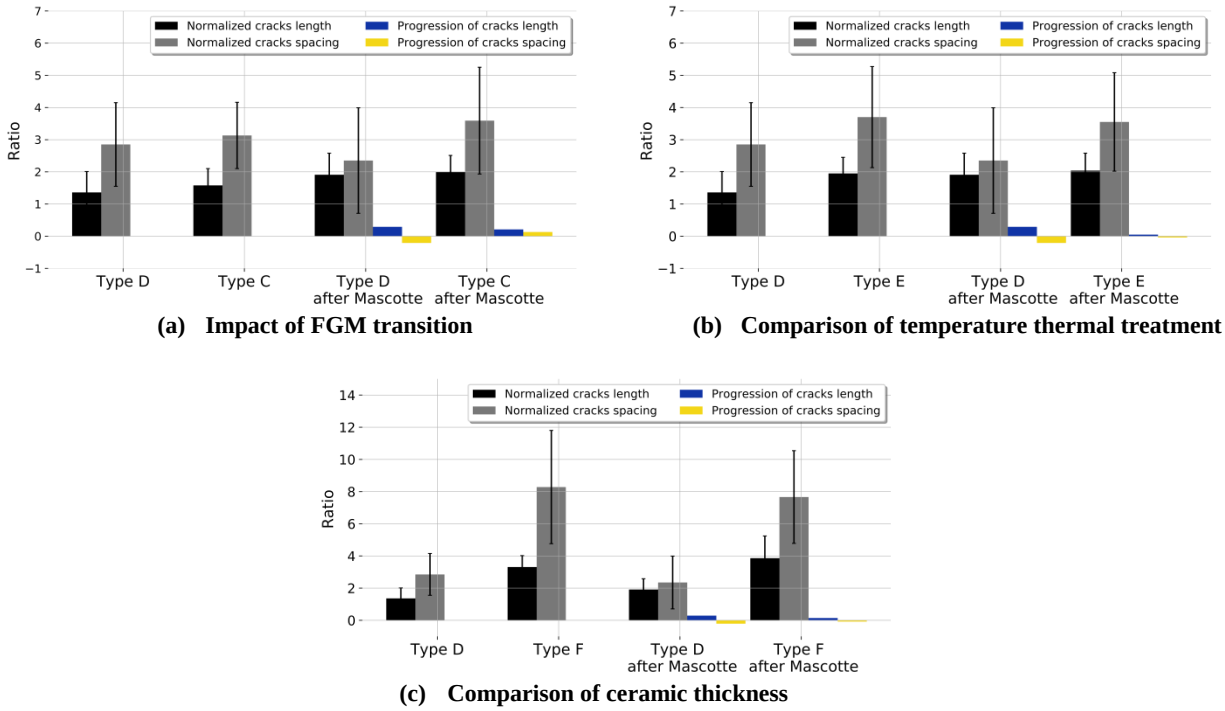


**(a) Impact of FGM transition**

**(b) Comparison of temperature thermal treatment**

**(c) Comparison of ceramic thickness**

**Figure 19 : Side-by-side comparison after Mascotte thermal cycling at flame temperature of 2000K (a) control sample versus sample type C, (b) control sample versus sample type E and (c) control sample versus type F**

After these first rounds of tests it is quite difficult to discriminate the samples, but some trends are showing up, like the temperature of thermal treatment and the necessity or not to have totally consolidated samples, and also their ceramic thickness.

## 4. Conclusion

Homogeneous gradient structures made of YSH and metal have been obtained by Plasma Spraying under air. The presence of inter-splat metal oxides was not an issue because of their easy elimination during an appropriate furnace thermal treatment. Moreover, despite the fact that samples contain two materials with a large difference in coefficient of thermal expansion, they exhibit a great resistance towards high temperature thermal cycling. The presence of vertical cracks due to the thermal treatment does not affect the performance and on they even allow a thermal stress relaxing, improving thermal shock resistance. Also, no oxidation was noticed even though the presence of vertical cracks. This could be explained by the compression stress during heating that closes these cracks.

Indeed, the mechanisms of cracks formation and propagation, in both environment tests (inert and oxidant atmosphere), correlate with previous studies. During heating, the top surface of sample is in large radial compressive stress state in which sintering and creep can induce non-linear deformation. During cooling, the radial stress becomes tensile whose magnitude is large enough to reach the fracture strength of ceramic leading to vertical cracks.
Moreover, the deflection of the cracks in the direction parallel to the surface plane appears when mode II stress intensity factor reach the value zero. Their coalescence will lead to spallation. Thus, it seems achievable to stop cracks propagation with optimised composition layers having high fracture strength. Currently measurements of mechanical properties of pure and composite compositions such as fracture strength and young modulus at high temperature are undergoing. They will allow proposing an optimised design combined to a numerical thermo-mechanical model and an optimisation algorithm.

Future performance tests will involve the use of the $CO_2$ laser test bench in a water vapour controlled atmosphere with high heat flux and various thermal cycling. Different designs and elaboration conditions will be tested by varying parameters such as the ceramic thickness (75, 150, 400, 800 µm), the thermal treatment (different maximum temperatures and pressures) and the gradient profile. This will allow discriminating some design parameters having an impact on the cracks propagation and possible oxidation.

**References**


[1] B. Reed, Advanced materials for radiation-cooled rockets, 1993. https://ntrs.nasa.gov/search.jsp?R=19940018579 (accessed May 23, 2019).

[2] A. Fortini, R. Tuffias, Advanced materials for chemical propulsion - Oxide-iridium/rhenium combustion chambers, in: 35th Jt. Propuls. Conf. Exhib., American Institute of Aeronautics and Astronautics, 1999. doi:10.2514/6.1999-2894.

[3] A. Fortini, R. Tuffias, J. Brockmeyer, B. Williams, R. Tuffias, J. Brockmeyer, B. Williams, A. Fortini, Comparative modeling and testing of radiation-cooled bipropellant combustion chambers, in: 33rd Jt. Propuls. Conf. Exhib., American Institute of Aeronautics and Astronautics, 1997. doi:10.2514/6.1997-2677.

[4] L. Schoenman, 4000 F materials for low-thrust rocket engines, J. Propuls. Power. 11 (1995) 1261–1267. doi:10.2514/3.23967.

[5] R. Tuffias, J. Brockmeyer, A. Fortini, B. Williams, A. Duffy, R. Kaplan, Engineering issues of iridium/rhenium rocket engines revisited, in: 35th Jt. Propuls. Conf. Exhib., American Institute of Aeronautics and Astronautics, n.d. doi:10.2514/6.1999-2752.

[6] N.R. Council, A Review of United States Air Force and Department of Defense Aerospace Propulsion Needs, 2006. doi:10.17226/11780.

[7] B.D. Reed, Testing of wrought iridium/chemical vapor deposition rhenium rocket - Missouri University of Science & Technology Library, (n.d.). http://link.library.mst.edu/portal/Testing-of-wrought-iridiumchemical-vapor/NO-8htfGSsY/ (accessed May 24, 2019).

[8] B.D. Reed, Evaluation of oxide-coated iridium-rhenium chambers, in: Monterey, CA, United States, 1994. https://ntrs.nasa.gov/search.jsp?R=19940024594 (accessed May 23, 2019).

[9] K. Zhang, S. Bai, L. Zhu, Y. Ye, H. Zhang, Y. Ai, S. Li, Y. Tang, Ablation and surface heating behaviors of graphite based Ir-Al coating in a plasma wind tunnel, Surf. Coat. Technol. 358 (2019) 371–377. doi:10.1016/j.surfcoat.2018.10.047.

[10] L. Zhu, G. Du, S. Bai, H. Zhang, Y. Ye, Y. Ai, Oxidation behavior of a double-layer iridium-aluminum intermetallic coating on iridium at the temperature of 1400°C–2000°C in the air atmosphere, Corros. Sci. 123 (2017) 328–338. doi:10.1016/j.corsci.2017.05.010.

[11] J. Buckley, Stabilization of the phase transformations in hafnium oxide, Retrosp. Theses Diss. (1968). doi:https://doi.org/10.31274/rtd-180813-4244.

[12] J. Wang, H.P. Li, R. Stevens, Hafnia and hafnia-toughened ceramics, J. Mater. Sci. 27 (1992) 5397–5430. doi:10.1007/BF00541601.

[13] A. Kawasaki, R. Watanabe, Thermal fracture behavior of metal/ceramic functionally graded materials, Eng. Fract. Mech. 69 (2002) 1713–1728. doi:10.1016/S0013-7944(02)00054-1.

[14] A. Kawasaki, R. Watanabe, Evaluation of thermomechanical performance for thermal barrier type of sintered functionally graded materials, Compos. Part B Eng. 28 (1997) 29–35. doi:10.1016/S1359-8368(96)00017-0.

[15] A. Kawasaki, R. Watanabe, Thermal Shock Fracture Mechanism of Metal/Ceramic Functionally Gradient Materials, in: G.A. Schneider, G. Petzow (Eds.), Therm. Shock Therm. Fatigue Behav. Adv. Ceram., Springer Netherlands, Dordrecht, 1993: pp. 509–520. doi:10.1007/978-94-015-8200-1_44.

[16] Z. Gan, H.W. Ng, Experiments and inelastic finite element analyses of plasma sprayed graded coatings under cyclic thermal shock, Mater. Sci. Eng. A. 385 (2004) 314–324. doi:10.1016/j.msea.2004.06.053.

[17] M. Naebe, K. Shirvanimoghaddam, Functionally graded materials: A review of fabrication and properties, Appl. Mater. Today. 5 (2016) 223–245. doi:10.1016/j.apmt.2016.10.001.

[18] A.H. Pakseresht, A.H. Javadi, E. Ghasali, A. Shahbazkhan, S. Shakhesi, Evaluation of hot corrosion behavior of plasma sprayed thermal barrier coatings with graded intermediate layer and double ceramic top layer, Surf. Coat. Technol. 288 (2016) 36–45. doi:10.1016/j.surfcoat.2016.01.012.

[19] Extreme Temperature Coatings for Future Gas Turbine Engines, ResearchGate. (n.d.). https://www.researchgate.net/publication/267504229_Extreme_Temperature_Coatings_for_Future_Gas_Turbine_Engines (accessed August 22, 2017).

DOI: 10.13009/EUCASS2019-346



[20] K.N. Lee, D.S. Fox, N.P. Bansal, Rare earth silicate environmental barrier coatings for SiC/SiC composites and Si3N4 ceramics, J. Eur. Ceram. Soc. 25 (2005) 1705–1715. doi:10.1016/j.jeurceramsoc.2004.12.013.
[21] K.A. Khor, Y.W. Gu, Thermal properties of plasma-sprayed functionally graded thermal barrier coatings, Thin Solid Films. 372 (2000) 104–113. doi:10.1016/S0040-6090(00)01024-5.
[22] K. Swaminathan, D.M. Sangeetha, Thermal analysis of FGM plates – A critical review of various modeling techniques and solution methods, Compos. Struct. 160 (2017) 43–60. doi:10.1016/j.compstruct.2016.10.047.
[23] R. Chiba, Y. Sugano, Optimisation of material composition of functionally graded materials based on multiscale thermoelastic analysis, Acta Mech. 223 (2012) 891–909. doi:10.1007/s00707-011-0610-z.
[24] Y.J. Noh, Y.J. Kang, S.J. Youn, J.R. Cho, O.K. Lim, Reliability-based design optimization of volume fraction distribution in functionally graded composites, Comput. Mater. Sci. 69 (2013) 435–442. doi:10.1016/j.commatsci.2012.12.003.
[25] P.L. Fauchais, J.V.R. Heberlein, M. Boulos, Thermal Spray Fundamentals: From Powder to Part, Springer US, 2014. https://www.springer.com/la/book/9780387283197 (accessed May 28, 2019).
[26] S. Zhao, Y. Zhao, B. Zou, X. Fan, J. Xu, Y. Hui, X. Zhou, S. Liu, X. Cao, Characterization and thermal cycling behavior of La2(Zr0.7Ce0.3)2O7/8YSZ functionally graded thermal barrier coating prepared by atmospheric plasma spraying, J. Alloys Compd. 592 (2014) 109–114. doi:10.1016/j.jallcom.2014.01.001.
[27] L. del Campo, D.D.S. Meneses, A. Blin, B. Rousseau, E. Véron, M. Balat-Pichelin, P. Echegut, High-Temperature Radiative Properties of an Yttria-Stabilized Hafnia Ceramic, J. Am. Ceram. Soc. 94 (2011) 1859–1864. doi:10.1111/j.1551-2916.2010.04336.x.
[28] J.A. Gan, C.C. Berndt, Review on the Oxidation of Metallic Thermal Sprayed Coatings: A Case Study with Reference to Rare-Earth Permanent Magnetic Coatings, J. Therm. Spray Technol. 22 (2013) 1069–1091. doi:10.1007/s11666-013-9955-2.
[29] M. Białas, Finite element analysis of stress distribution in thermal barrier coatings, Surf. Coat. Technol. 202 (2008) 6002–6010. doi:10.1016/j.surfcoat.2008.06.178.
[30] T.W. Clyne, Residual Stresses in Surface Coatings and Their Effects on Interfacial Debonding, Key Eng. Mater. (1996). doi:10.4028/www.scientific.net/KEM.116-117.307.
[31] D. Zhu, Environmental Barrier Coating Fracture, Fatigue and High-Heat-Flux Durability Modeling and Stochastic Progressive Damage Simulation, (2017). https://ntrs.nasa.gov/search.jsp?R=20180000359 (accessed June 17, 2019).
[32] A.G. Evans, G.B. Crumley, R.E. Demaray, On the mechanical behavior of brittle coatings and layers, Oxid. Met. 20 (1983) 193–216. doi:10.1007/BF00656841.
[33] A.J. Fortini, R.H. Tuffias, The next step in chemical propulsion: Oxide-iridium/rhenium combustion chambers, AIP Conf. Proc. 458 (1999) 691–696. doi:10.1063/1.57716.